Inorganic Chemistry

Article

pubs.acs.org/IC

Nanoporous Delafossite $CuAlO_2$ from Inorganic/Polymer Double Gels: A Desirable High-Surface-Area p-Type Transparent Electrode Material

Barun Das,[†] Adèle Renaud,[†] Alex M. Volosin,[†] Lei Yu,[‡] Nathan Newman,[‡] and Dong-Kyun Seo*,[†]

[†]Department of Chemistry and Biochemistry, Arizona State University, Tempe, Arizona 85287-1604, United States

[‡]School for Engineering of Matter, Transport and Energy, Arizona State University, Tempe, Arizona 85287-6106, United States

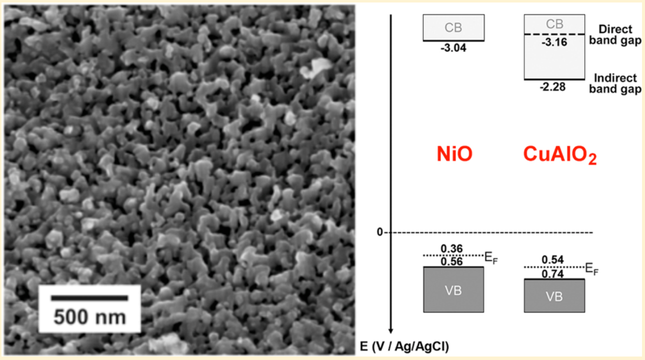

ABSTRACT: Nanoporous structures of a p-type semiconductor, delafossite $CuAlO_2$, with a high crystallinity have been fabricated through an inorganic/polymer double-gel process and characterized for the first time via Mott–Schottky measurements. The effect of the precursor concentration, calcination temperature, and atmosphere were examined to achieve high crystallinity and photoelectrochemical properties while maximizing the porosity. The optical properties of the nanoporous $CuAlO_2$ are in good agreement with the literature with an optical band gap of 3.9 eV, and the observed high electrical conductivity and hole concentrations conform to highly crystalline and well-sintered nanoparticles observed in the product. The Mott–Schottky plot from the electrochemical impedance spectroscopy studies indicates a flat-band potential of 0.49 V versus Ag/AgCl. It is concluded that $CuAlO_2$ exhibits band energies very close to those of NiO but with electrical properties very desirable in the fabrication of photoelectrochemical devices including dye-sensitized solar cells.

1. INTRODUCTION

Nanostructured transparent conducting oxides (TCOs) are a new class of multifunctional materials for emerging applications in the area of photoelectrochemical solar energy production,[1] biosensors,[2] and electrooptical devices,[3] where the materials are fabricated in nanoporous forms and utilized as high-surface-area electrodes, beyond the conventional applications with dense films.[4−7] For example, mesoporous antimony-doped tin oxide (ATO) materials have been synthesized through a liquid-crystal template method for the fabrication of electroluminescence devices.[7] In other work, highly conductive mesoporous ATO has been produced in a two-step method by first synthesizing ATO nanoparticles through a sol−gel route and subsequently using a block copolymer soft template.[8] Similarly, nanoporous indium−tin oxide (ITO) films have been prepared by spin-coating a suspension of ITO nanoparticles (~40 nm) onto planar substrates to host organic dyes[9] or Photosystem II.[10] In our previous studies, we have developed a simple one-pot sol−gel method that provides highly mesoporous transparent ATO materials, either in bulk or in films,[11,12] whose pore sizes could be controlled conveniently by varying the precursor concentrations. It has also been demonstrated that the synthesized nanoporous ATO materials are size-selective in incorporating DNA origami supercage structures[13] and that the materials are effective in electron transfer with Cyt-*c*[14] and with Fe^{2+}/Fe^{3+} redox pairs.[12]

Most of the TCOs employed for the reported syntheses have n-type charge carriers, while it would be equally important to fabricate nanoporous materials from p-type TCOs. Delafossite-type Cu^+-containing oxides, $CuMO_2$ ($M = B^{3+}, Al^{3+}, Ga^{3+}, Cr^{3+}, Y^{3+}$, etc.), are among the few known p-type TCOs.[15,16] For example, $CuAlO_2$ shows a direct band gap of 3.5 eV,[15] and thin films of the compound exhibited room temperature (RT) p-type conductivity up to 1 $S \cdot cm^{-1}$.[16] While various synthetic methods have been employed, including high-temperature solid-state reaction,[17−19] hydrothermal routes,[20,21] sol−gel processes[22−26] and ion exchange,[27] synthesis of $CuAlO_2$ with a nanoporous structure has been challenging. Sol−gel processes are generally successful in producing nanoporous materials, with three-dimensionally (3D) interconnected gel network structures of nanoparticles with textural porosity.[28,29] However, the high crystallinity and sintering required for the desired electrical properties are achieved usually under high-temperature conditions (~1000 °C),[30] which often leads to uncontrolled collapse of the pore structures.[31,32] Indeed, the high temperatures required for crystallization of $CuAlO_2$ with high purity have resulted in products with highly fused nanoparticles and thus with a negligible porosity.[22−26] Therefore, challenges still remain in the production of $CuAlO_2$ or others into a material having a nanoporous structure with a high surface area.

Special Issue: To Honor the Memory of Prof. John D. Corbett

Received: October 4, 2014
Published: January 13, 2015

DOI: 10.1021/ic5023906
Inorg. Chem. 2015, 54, 1100−1108

Herein, we report the production and characterization of a nanoporous delafossite $CuAlO_2$ material with significant porosity and excellent electrical properties. The success of the method stems from the synthetic design in which the inorganic gel network structure is buttressed by the interpenetrating polymer gel network during drying and heat treatment.[11,12] The optical, electrical, and electrochemical characterizations have proven that our material is promising for different photoelectrochemical applications. The thermal stability of the porous structure of the resulting $CuAlO_2$ material was also examined at different temperatures.

2. EXPERIMENTAL SECTION

2.1. Materials Synthesis. Multiple samples were prepared at different calcination temperatures. In a typical synthesis, the material was prepared by dissolving 8.0 g of $Cu(NO_3)_2 \cdot 2.5H_2O$ (Baker Analyzed, 99.9%) and 11.5 g of $Al(NO_3)_3 \cdot 9H_2O$ (Sigma-Aldrich, 99%; mole ratio Cu/Al = 1.1) in 11.05 g of deionized water, followed by the addition of 29.25 g of absolute ethanol (Decon, 100%) to the aqueous solution in a polypropylene container. After ultrasonication for several minutes, 2.5 g of resorcinol (Sigma-Aldrich, 99%) and 3.7 g of a 37% (w/w) formaldehyde solution (Sigma-Aldrich; 7−8% methanol as the stabilizer) were added to the Cu^{2+}/Al^{3+} nitrate solution. A total of 10 g of propylene oxide (Alfa Aesar, 99+%) was then added slowly to the solution and sonicated for 2 min. The solution was sealed and kept at RT for gelation. After 3−4 h, the solution became a deep-green monolithic gel. The gel was further kept at RT for 1 day for aging. Subsequently, the gel was heated in a laboratory oven at 70 °C for 3 days, after which the gel became a hard red-brown monolith with some small cracks, which indicated polymerization of resorcinol and formaldehyde.

The monolithic composite gel was then removed and broken up into small pieces prior to drying in air for 1 day. Drying caused the composite materials to shrink noticeably. The small pieces were then calcined in an ashing furnace for 10 h at 500 °C, which produced a black powdery material. This black powder was then annealed in an argon atmosphere for 4 h in a tube furnace at different temperatures (850, 900, 950, 1000, and 1050 °C) to produce a violet-blue powder material. The samples were named CAO-850, CAO-900, CAO-950, CAO-1000, and CAO-1050 by following the annealing temperatures used for each sample. In order to investigate the role of resorcinol/formaldehyde polymeric networks on the porosity of the products, we prepared another sample without adding the polymer precursors. The same synthetic procedure was followed, and the calcined product was annealed at 900 °C. The resulting sample is denoted as CAO-REF hereafter.

2.2. Materials Characterization. Nitrogen sorption isotherms were collected on a Micromeritics ASAP 2020 surface area and porosity analyzer at 77 K. Samples were degassed under vacuum at 200 °C for 2 h, followed by 300 °C for 6 h. For surface area calculation, the Brunauer−Emmett−Teller (BET) model was applied to the adsorption branch in the partial pressure (p/p_0) range of 0.05−0.2, and all samples showed the C value in the range from 90 to 140. For pore size distributions, the Barrett−Joyner−Halenda (BJH) model was applied to the desorption branch with the Halsey thickness curve[33] for nonuniform surfaces and Faas correction[34] to account for multilayer desorption in adsorbed layer thickness estimation. The total pore volume was estimated from the total quantity of gas adsorbed at the data point closest to p/p_0 of 0.98 using the desorption branch. The same procedure was applied for both powder and pelleted samples. The pelleted samples were crushed coarsely into small pieces before measurements in order to improve the gas sorption kinetics without creating additional mesoporosity. The total open porosity of the pelleted samples was estimated from water pycnometry using the crushed samples.

Powder X-ray diffraction (XRD) data were collected using a Siemens D5000 diffractometer with Cu Kα radiation with silicon as an internal standard. Scanning electron microscopy (SEM) studies were carried out with ground samples using an FEI XL-30 environmental scanning electron microscope with 30 keV electrons. For transmission electron microscopy (TEM) studies, samples were prepared by grinding samples in absolute ethanol to form a dispersion. A TEM grid was dipped into the dispersion, taken out, and dried in air. High-resolution TEM images were collected on a JEOL 2010F microscope at an accelerating voltage of 200 kV.

X-ray photoelectron spectroscopy (XPS) studies were carried out using a VG-220IXL spectrometer with monochromatic Al Kα radiation (1486.6 eV, line width 0.8 eV). The pressure in the analysis chamber was kept at the level of 10^{-9} Torr while the spectra were recorded. The spectrometer had an energy resolution of 0.4 eV. All of the binding energies were corrected with the C 1s binding energy at 285.0 eV. The optical properties of the products were investigated using a PerkinElmer Lambda-8 UV−vis spectrophotometer with a reflectance spectroscopy accessory to collect diffuse-reflectance UV−vis spectra. The sample was ground for a few minutes and loaded into a custom sample holder, and the spectra were collected at an interval of 4 nm at a scan rate of 120 nm·min^{-1} with a slit size of 3 nm.

For conductivity measurement, about 0.1 g of ground powder was pressed into a pellet (1 cm diameter and ~0.5 mm thickness) at 6000 psi and subsequently heated at 200 °C overnight in an argon atmosphere to remove the adsorbed moisture, which otherwise may affect the measurements. Four evenly spaced (2.5 mm spacing) spring-loaded pogo pins were pressed firmly onto the pellet. The current was supplied to the two outermost pins using a Keithley 6221 current source, and the voltage between the two inner pins was measured differentially using a Keithley 2000 multimeter. The resistivity (R) was calculated from $R = 4.53\ Vt/I$, where V, t, and I are the voltage, the thickness of the pellet, and the current, respectively.[35] The equation holds well for a thin-film or pellet configuration where $2t \leq s$, where t and s are the thickness of the pellet and the spacing between the probes, respectively. The temperature was varied by slowly lowering the measurement assembly into liquid helium and measured using a calibrated silicon diode sensor. Both the sample and diode sensor were kept in good thermal contact with a thin block of copper.

The flat-band potential position and charge-carrier density were determined on pellets by electrochemical impedance measurements using the Mott−Schottky method. The pellets were prepared by pressing a well-ground sample powder at approximately 6000 psi and subsequent heating at 340 °C during 3 h in air. For the measurements, an electrochemical cell was built with three electrodes (an Ag/AgCl reference electrode, a platinum counter electrode, and a working electrode) immersed in a $LiClO_4$ (1 M) aqueous solution (pH = 7.2). The working electrode was fabricated by attaching a sample pellet with a copper wire using a carbon paste for a good electrical contact. This contact was then cured and sealed off with an epoxy resin (CaldoFix-2 kit, Struers), and the pellet surface was polished (SiC paper, grid 1200 and 4000) to obtain a smooth electrode surface. An alternating-current voltage (5 mV in amplitude and a frequency range of 1−10 kHz) was imposed in a potential range of −0.2 to −0.7 V versus Ag/AgCl using a galvanostat/potentiostat from CH Instruments (model 600D series). Subsequently, the interface semiconductor/electrolyte capacitance (C) was determined according to the imposed potential (E) using a simplified Randles equivalent circuit (see below) by assuming that the faradaic part can be neglected at high frequency[36] and that the series resistance is composed mainly of the contact resistance and resistance of the electrolyte. The constant phase element (CPE) was given as $Z_{CPE} = 1/Q(j\omega)^{\alpha}$, where $0 < \alpha < 1$, reflecting the nonideality of the interface capacitance. The C values for an applied potential were calculated using $C = (R_s^{1-\alpha}Q)^{1/\alpha}$.[37,38] The flat-band potential (E_{fb}) and charge-carrier density (N_C) were then deduced from the Mott−Schottky plot (C_{SC}^{-2} vs E), which utilizes the Mott−Schottky equation for a p-type semiconductor: $1/C_{SC}^2 = (-2/\varepsilon\varepsilon_0 e A^2 N_C)(E - E_{fb} + kT/e)$, where C_{SC} is the capacitance in the space charge region of the semiconductor, A the interfacial surface area between the semiconductor electrode and electrolyte, k the Boltzmann constant, T the temperature, e the electron charge, ε_0 the vacuum permittivity, and ε the relative permittivity of the semiconductor. For the calculations, C_{SC}^{-2} was approximated to be C^{-2} due to the large capacitance of the

Helmholtz layer, at the semiconductor surface in the electrolyte, in comparison to C_{SC}.

3. RESULTS AND DISCUSSION

Figure 1 illustrates the overall synthetic procedure in which the nanoporous $CuAlO_2$ material is produced by first creating, drying, and calcining inorganic/polymer composite gels that exhibit a 3D interpenetrating network structure. The composite gels are synthesized by forming a hydrous alumina gel network followed by promotion of polymeric resorcinol/formaldehyde gel formation. The synthesis is carried out by first mixing all of the reaction precursors in one pot. The solution is acidic ($pH < 2$) because of the hydrolysis of $Al(NO_3)_3{\cdot}9H_2O$ and consequent generation of nitric acid. At ambient temperature, the propylene oxide gradually consumes the nitric acid by an addition reaction,[39] which increases the pH of the solution and thus induces uniform formation of an inorganic gel network (top left in Figure 1). The resulting inorganic gel was deep green because of the Cu^{2+} ions, which are present more likely in the liquid portion of the gel, instead of cogelling with Al^{3+} in the inorganic gel network. It has been shown that alumina gels prepared from the nitrate precursor through this acid scavenger method are comprised of amorphous spherical particles with diameters in the 5−15 nm range that are amorphous.[39] The inorganic gel was then heated at 70 °C to induce resorcinol/formaldehyde polymerization in the pore liquid of the gel, resulting in an inorganic/polymer composite gel consisting of interpenetrating networks of alumina and a polymer with a dark-red-brown color due to the formation of *o*-methide quinones as a byproduct (top right in Figure 1).[22] The composite gel was dried for the following high-temperature calcination and annealing (see below). During drying, the Cu^{2+} ions present in the pore liquid homogeneously precipitate and are distributed throughout the body of the dried composite gel. Such an intimate mixing in the nanoscale has been found to be important for more homogeneous $CuAlO_2$ products, as reported in the literature,[40] where γ-AlOOH/Cu(acetate) nanocomposites were prepared by drying a sol solution containing both γ-AlOOH nanorods and dissolved Cu(acetate) in order to produce dense thin films.

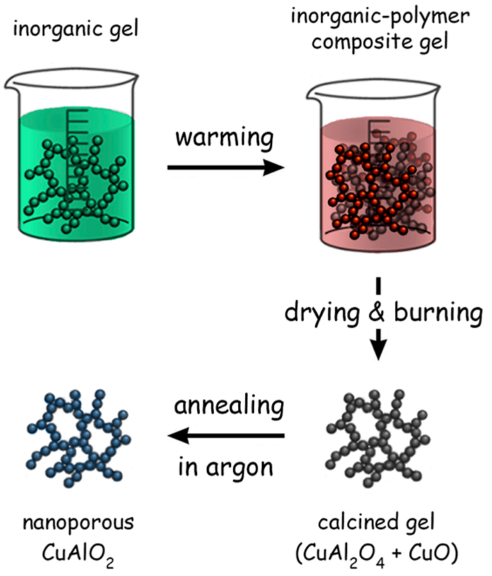

Figure 1. Synthetic scheme of the nanoporous $CuAlO_2$ materials.

Calcination of the gels at 500 °C in air leads to a fully oxidized gel material that consists of crystalline $CuAl_2O_4$ and CuO, after the polymer component is burned off (bottom right in Figure 1). Formation of $CuAlO_2$ (bottom left in Figure 1) was then achieved by subsequent annealing of the calcined gel material in an argon flow at various temperatures from 850 to 1050 °C. The annealing allowed the solid-state reaction $CuAl_2O_4(s) + CuO(s) \rightarrow 2CuAlO_2(s) + {}^1/{}_2O_2(g)$ in which Cu^{2+} ions are reduced autonomously to Cu^+. Thermodynamics and phase equilibria of $CuAlO_2$ and $CuAl_2O_4$ indicate that the solid-state reaction can take place only above ∼1000 °C if annealed in air (oxygen partial pressure = 0.21 atm).[28] In recent studies,[41] the annealing temperature could be lowered by almost 100 °C to 920 °C when annealing took place in an inert atmosphere. Although not detailed here, however, our preliminary results showed that when the Cu and Al precursors are stoichiometrically present in the material, the reaction was complete only above 1000 °C and the pore structure collapsed completely at such a high temperature, leading to a negligible nanoporosity. Further exploration of the synthetic conditions has shown that the reaction can be complete at temperatures as low as 900 °C if the Cu is present in excess and later the Cu/Al atomic ratio was optimized at 1.1. This is in agreement with a quite recent report that phase-pure $CuAlO_2$ powder could be prepared by a single annealing by using an excess of CuO.[42] However, the employed Cu/Al ratio was much higher at 3, which may be due to the fact that annealing was carried out in air in the studies. For our purpose, the lower temperature reaction condition was critical because it afforded much less significant pore collapse. After complete formation of $CuAlO_2$, the leftover copper oxides (CuO and/or Cu_2O) could be easily removed by soaking the annealed material in concentrated HCl, followed by washing and drying.

Figure 2 shows the powder XRD patterns of the final products annealed at 850, 900, 950, 1000, and 1050 °C, along with the simulated pattern for $CuAlO_2$.[17] In contrast to the rest of the samples, the presence of the $CuAl_2O_4$ peaks (marked with the black inverse triangle symbol) in CAO-850 indicates that the formation of $CuAlO_2$ is not complete at 850 °C given the annealing period. All of the other samples are pure

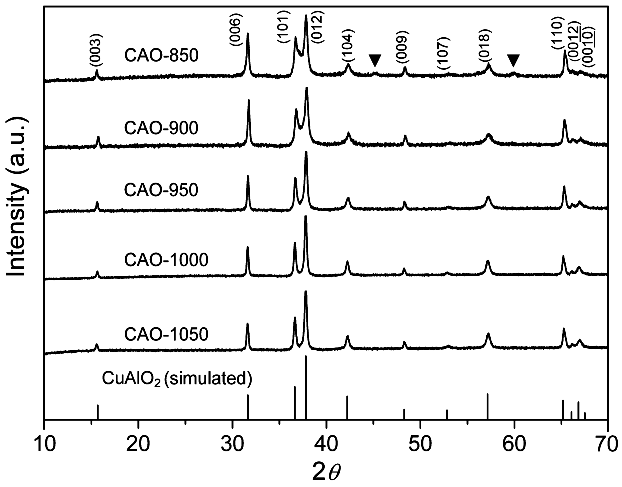

Figure 2. Powder XRD patterns of the samples prepared using the scheme in Figure 1 at different annealing temperatures (850, 900, 950, 1000, and 1050 °C). The Bragg peaks from the $CuAl_2O_4$ (spinel) phase are marked with black inverse triangles.

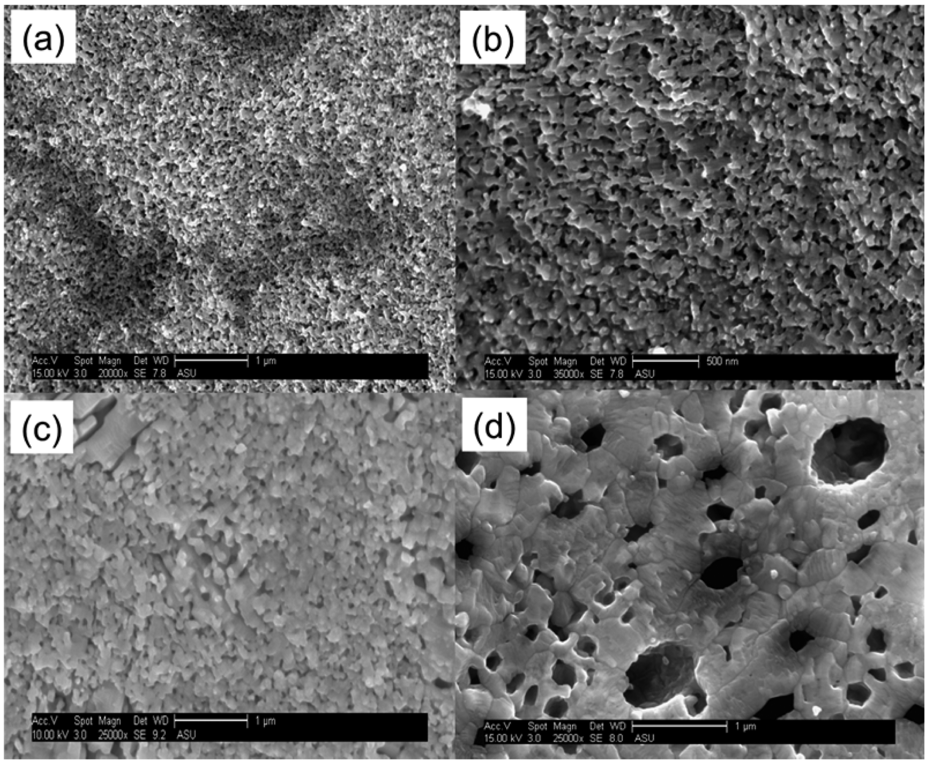

Figure 3. SEM images of (a and b) CAO-900 in different magnification ratios and (c) CAO-1050 and (d) CAO-REF. The scale bars are 1 μm in parts a, c, and d and 500 nm in part b.

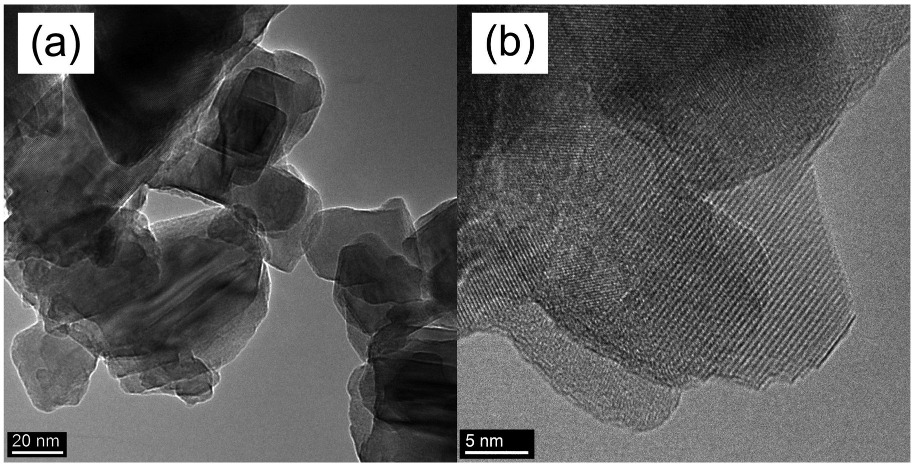

Figure 4. TEM images of CAO-900. The scale bars are 20 nm in part a and 5 nm in part b.

according to their XRD patterns. The Bragg peaks become significantly sharper as the annealing temperature increases, which may be due to the particle growth and improved crystallinity. The low-magnification SEM image of CAO-900 in Figure 3a clearly shows a uniformly corrugated surface with a textural porosity. The higher magnification image in Figure 3b indicates that the particles of 50−100 nm in size are well sintered with significant neck formation. The TEM images of CAO-900 in Figure 4 corroborate with these observations in that highly crystalline nanoparticles have sizes in the range of 30−100 nm, while the degree of particle consolidation cannot be determined by inspection of the images. These particles are much larger than the reported primary particles of the alumina gel network of the composite gel[39] that was prepared in the beginning steps of the synthetic procedure, which is due to the high-temperature annealing condition. It is noted that nanoparticles of $CuAlO_2$ have been synthesized previously with smaller crystalline domain sizes (~35 nm) at a temperature as low as 775 °C using a sol−gel route, and yet that controlled mesoporosity of the materials has not been demonstrated in the literature.[43] The high-temperature condition required for pure-phase formation can be a significant challenge because the pore structure can collapse during heating, as shown in our studies.

The effect of the annealing temperature can be seen directly from the SEM image of CAO-1050 (Figure 3c). The sintering of the particles is much more significant than what is found in CAO-900 because structural features in the range of 100−500 nm are evident in the SEM image. In comparison to Figure 3a−c, Figure 3d shows a much denser surface, which is pecked with large pits. The sample in the image is CAO-REF in Table 1; the

Table 1. Surface Area, Pore Characteristics, RT Electrical Conductivity, and Electrical Band Gap of the Products

sample	BET surface area ($m^2 \cdot g^{-1}$)	pore volume ($cm^3 \cdot g^{-1}$)	pore width[a] (nm)	conductivity at RT ($mS \cdot cm^{-1}$)	E_a (eV)
CAO-900	12	0.099	35	0.15	0.23
CAO-950	5.6	0.051	37	0.94	0.22
CAO-1000	3.2	0.023	28	2.0	0.21
CAO-1050	3.1	0.022	30	3.0	0.21
CAO-REF	2.6	0.013	14		

[a] 4(pore volume)/(BET surface area).

$CuAlO_2$ product annealed at 900 °C but without using the resorcinol and formaldehyde polymer precursors in the initial precursor solution. In contrast to CAO-900 and CAO-1050, the almost complete collapse of gel pores in the sample clearly confirms the benefit of our synthetic strategy based on the interpenetrating inorganic/polymer gel network formation.

Nitrogen sorption isotherms and the corresponding BJH pore distributions are shown in Figure 5 for all of the pure CAO samples (CAO-900, -950, -1000, and -1050). Estimated BET surface areas and average pore widths are also listed in Table 1. The presence of mesopores in all of these samples is evident from hysteresis loops in the isotherms. The isotherms do not show a clear saturation of adsorption near $p/p_0 = 1$, perhaps indicating the copresence of macropores. The CAO-900 sample showed the highest BET surface (12 $m^2 \cdot g^{-1}$) with a total pore volume of 0.1 $cm^3 \cdot g^{-1}$ and an average pore size of 35 nm. As the annealing temperature increases, the BET surface area and pore volume decrease drastically both by a factor of about 4 (Figure 6) up to 1000 °C and remain the same, indicating more or less complete sintering and pore collapse up to that temperature. Meanwhile, the peak in the BJH pore distribution gradually shifts to a larger pore size, and at the same time, it becomes significantly broader, which is understandable based on the consolidation of the particles and pore collapse. CAO-REF shows the least nanoporosity in Table 1, and this is consistent with the most densified nature of the material, as observed in Figure 3d.

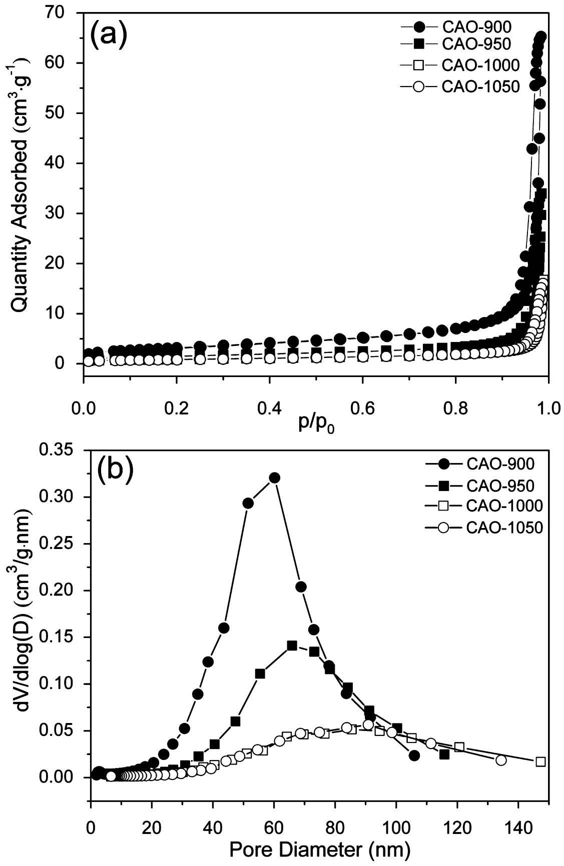

Figure 5. (a) Nitrogen sorption isotherms and (b) BJH pore distributions of the samples prepared using the scheme in Figure 1 at different annealing temperatures (900, 950, 1000, and 1050 °C).

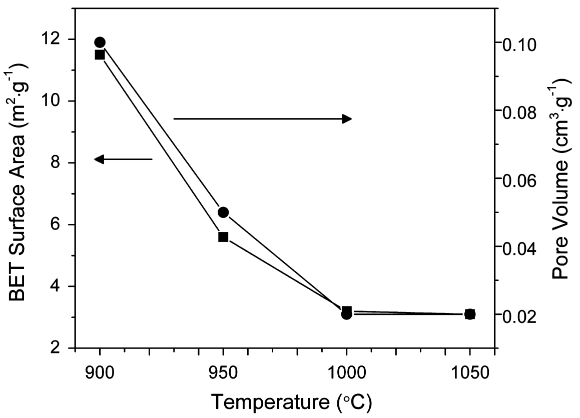

Figure 6. BET surface areas and pore volumes of the samples prepared using the scheme in Figure 1 at different annealing temperatures (900, 950, 1000, and 1050 °C).

Parts a and b of Figure 7 show the spectral regions of the Cu 2p and O 1s binding energy, respectively, in the high-resolution XPS spectrum of CAO-900. The binding energies of Cu $2p_{3/2}$ (931.9 eV) and Cu $2p_{1/2}$ (951.7 eV) and the O 1s binding energy (530.3 eV) are consistent with literature values for $CuAlO_2$.[44] Cu^{2+} ions as in $CuAl_2O_4$ or CuO are absent in the sample, which otherwise would have been indicated by the presence of peaks around 933.8[45] and 953.7 eV.[46] This is in agreement with the lack of the satellite or "shake-up" peak around 943 eV typically associated with Cu^{2+}.[47] However, the weak-intensity peak at 937 eV in Figure 7a has been assigned as Cu $2p_{3/2}$ of the Cu^{2+} ions self-doped in a small amount in the structure of $CuAlO_2$. The unusually high binding energy for Cu^{2+} has been attributed to the lower coordination number and short Cu−O bond length (1.86 Å) in the $CuAlO_2$ structure.[48]

The optical properties of the samples were studied by collecting and analyzing their diffuse-reflectance spectra in the UV−vis region. Figure 8a shows the Kubelka−Munk (K−M) transform of the reflectance spectrum for CAO-900 in the spectral wavelength range from 200 to 800 nm. While the fundamental absorption starts at 400 nm, the sample shows a broad weak absorption peak centered around 690 nm (∼1.8 eV), which has been reported to indicate the presence of an indirect band gap.[15,16] In more recent studies, however, it has

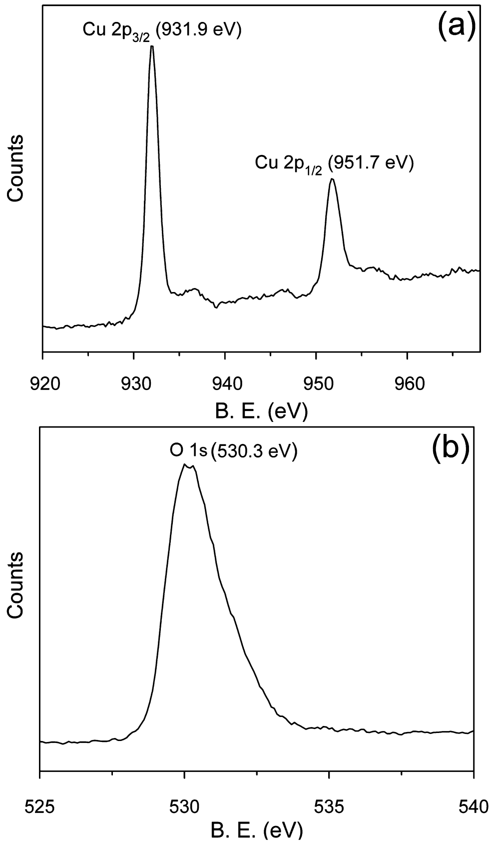

Figure 7. High-resolution XPS spectra in the binding energy regions of (a) Cu $2p_{3/2}$ and Cu $2p_{1/2}$ and (b) O 1s of CAO-900.

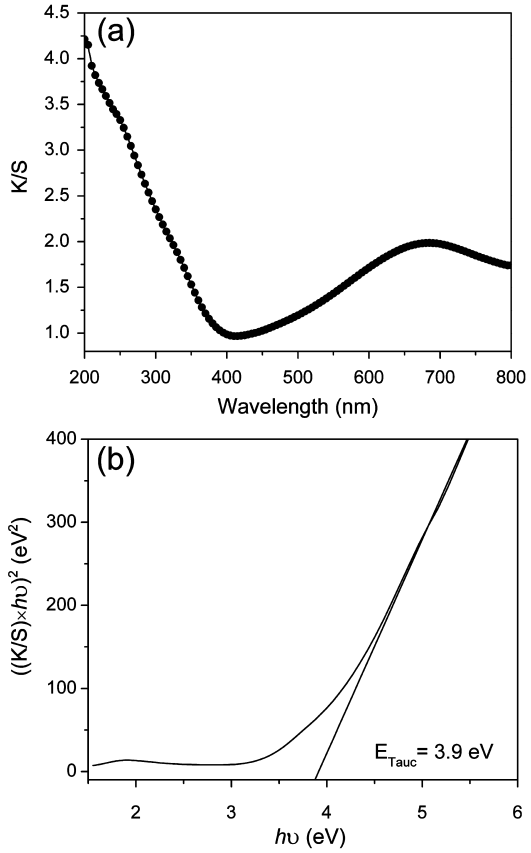

Figure 8. (a) K–M transform of UV–vis diffuse-reflectance spectrum and (b) Tauc plot of $[(K/S)h\nu]^2$ versus $h\nu$ of CAO-900.

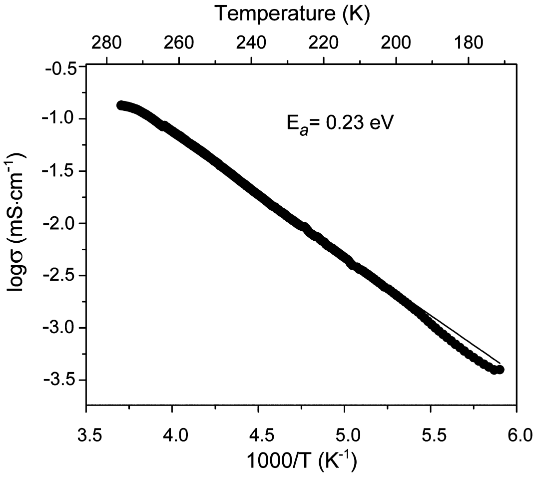

Figure 9. Logarithm of electrical conductivity versus reciprocal temperature for CAO-900 pelleted at 6000 psi. The electrical band gap (E_a) is estimated to be 0.23 eV in the higher-temperature region.

been assigned to a d–d transition of Cu^{2+} ions present in the compound, based on first-principle electronic structure calculations and the fact that the absorption energy does match the typical crystal-field split d states of Cu^{2+} ions.[49,50] These ions are more likely the self-doped Cu^{2+} ions observed in the XPS spectra discussed above. The same works indicate the presence of an indirect band gap near 3.0 eV, which is consistent with the onset of absorption around 410 nm (3.02 eV) observed in Figure 8a. When the corresponding Tauc plot of $[(K/S)h\nu]^2$ versus $h\nu$ in Figure 8b was used, the direct optical band gap of the sample was estimated to be about 3.9 eV (~320 nm). The Tauc direct band gap of $CuAlO_2$ is in the range from 3.5 to 3.9 eV in the literature,[15,44,51] and our value is consistent with the one for the products prepared through a sol–gel process.[44]

Figure 9 shows the logarithm of conductivity as a function of the reciprocal temperature for pelleted CAO-900 measured at 170–280 K. The monotonic increase of the conductivity with increasing temperature indicates a semiconducting behavior of the material. The activation energy was estimated to be 0.23 eV in the linear region above 200 K in Figure 9 using the Arrhenius equation. Although not shown, all of the other samples showed the same linear behavior in their logarithm of conductivity versus temperature graphs. Their RT conductivity and electrical band gaps are listed in Table 1. The conductivity increases drastically as the annealing temperature increases among the samples by a factor of up to 20 from 0.15 to 3.0 mS·cm^{-1}, while the electrical band gap remains more or less the same (0.21–0.23 eV). The electrical band-gap values are in agreement with the literature.[15,16] The increase in the conductivity is understandable because the samples annealed at higher temperatures showed a lesser porosity, a higher degree of sintering, and a higher crystallinity. The electrical band gap would not be affected by the annealing temperature because it is an intrinsic nature of the compound, as found in our results.

Parts a and b of Figure 10 show the simplified equivalent circuit used for our data analysis and the Mott–Schottky plot obtained for CAO-900 pellets, respectively. Although not detailed here, the premeasured mesoporosity of the pellets was approximately the same as that of the powder, indicating that the innate electrical and electrochemical properties of the

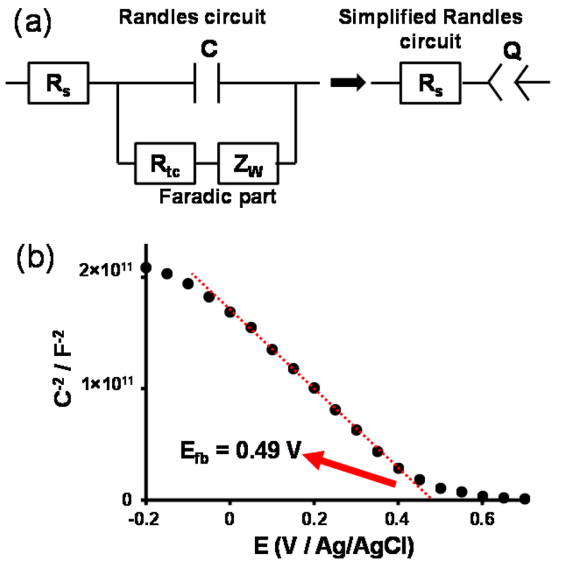

Figure 10. (a) Randles circuit where R_{tc} is the transfer charge resistance and Z_W is the Warburg impedance due to diffusion phenomena. Q corresponds to the CPE in the simplified equivalent circuit. (b) Mott–Schottky plot for the CAO-900 pellet (electrolyte: $LiClO_4$ in water; pH = 7.2). The flat-band potential was calculated at T = 25 °C, and the charge-carrier density was deduced from the slope value with a surface area (A) of 0.9 cm^2 and a dielectric constant of $CuAlO_2$ of 10.[58]

pellets are a good representation of the nanostructured particles, while the total open porosity of the pelleted sample was about 31 vol % from the water pycnometry. The plot shows a linear relationship for C_{SC}^{-2} versus E with a negative slope, which indicates a p-type behavior under depletion conditions.[52] By extrapolation to C^{-2} = 0, therefore, the Mott–Schottky equation indicates a flat-band potential of 0.49 V/Ag/AgCl in the measurement condition (pH of 7.2 with T = 25 °C). This value is in excellent agreement with the literature, although the previous measurements were carried out using different techniques such as photoelectron spectroscopy in air,[53] photocurrent–potential, or potentiodynamic measurements.[54,55] In addition, the charge-carrier density (N_C) was estimated from the slope in the Mott–Schottky plot. After the value was corrected with the measured open porosity of the pelleted sample by following the literature,[56,57] the calculated value was 3×10^{19} cm^{-3}, which is notably high and, in fact, represents one of the best values obtained for $CuAlO_2$,[16,58] indicating the excellent electrical properties of nanoporous $CuAlO_2$. In comparison, for example, the best charge-carrier density around 2.7×10^{19} cm^{-3} has been reported for high-quality thin films.[58] It is noted that the Mott–Schottky measurements were carried out on a pressed pellet, which was heat-treated at 340 °C for 3 h in order to provide significant contact among the nanoporous aggregates. The individual aggregates themselves consist of the primary nanoparticles that are strongly consolidated, as observed in their SEM images (Figure 3). Such a network structure can support the depletion layer, and this is clearly evidenced by the linear behavior in the Mott–Schottky plot in Figure 10a, showing a classical feature for p-type semiconductors under depletion conditions. The same conclusions have been made from the Mott–Schottky measurements for $CuGaO_2$ in similar conditions.[57] The material exhibits almost the same flat-band potential as $CuAlO_2$. The estimated depletion layer width was about 60 nm for the charge-carrier density value of 10^{17} cm^{-3} and about 6 nm for 9×10^{19} cm^{-3}. Given the higher conductivity of $CuAlO_2$ (3×10^{19} cm^{-3}) in our study, the depletion layer width would be shorter than the particle size (30–100 nm) found in our products.

Figure 11 compares the band positions of $CuAlO_2$ with those of two other p-type semiconductors, NiO[38,59] and $Cu_5Ta_{11}O_{30}$,[60] which have been utilized in photoelectrochemical systems. For the sake of comparison with those compounds, the band positions of $CuAlO_2$ were estimated at a common pH value of 6.3 by considering the Nernstian relation (an increment of 0.059 V/pH at 25 °C and 1 atm) under the assumption that H^+ and OH^- are potential determining ions adsorbed on the solid surface within the Helmholtz layer[61] and, furthermore, by assuming that the difference of the potential between the valence band and Fermi level is around 0.2 V, a typical value for p-type semiconductors.[62] It is cautioned that the band-edge values shown in Figure 11 should be considered as a general guideline for future experiments, partly because of the approximations used for their estimation and also because of the varying experimental parameters in different photoelectrochemical applications of the material. Nevertheless, the valence-band-edge positions are very similar between $CuAlO_2$ and $Cu_5Ta_{11}O_{30}$, as we expect from the fact that the top of the valence bands consists mainly of Cu 3d orbitals with a formal $3d^{10}$ electron configuration with some O 2p orbital contributions for Cu^+ in both compounds.[16,60,63] However, the larger band gap of $CuAlO_2$ makes its conduction band edge located at a higher energy. In fact, Figure 11 shows that the resulting band-energy positions of $CuAlO_2$ are closer to those of NiO, one of the most employed p-type semiconductors in the fabrication of dye-sensitized solar cells and photoelectrochemical devices for water splitting. The high electrical conductivity and carrier concentration found in nanoporous $CuAlO_2$ make the material useful for those applications.

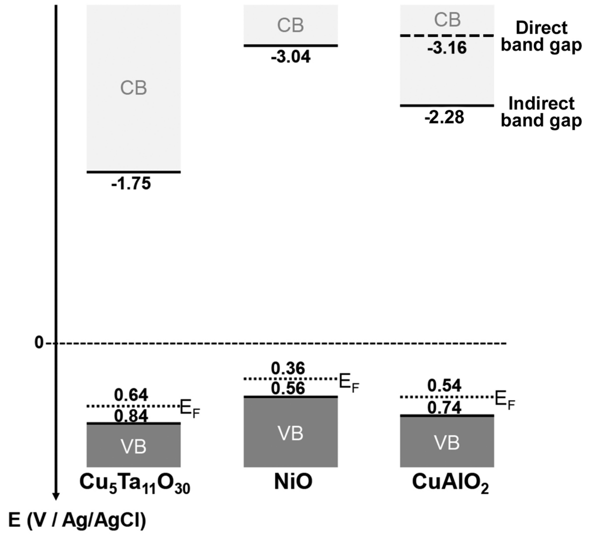

Figure 11. Comparison of the positions of the band energies for $Cu_5Ta_{11}O_{30}$,[55] NiO,[38,54] and $CuAlO_2$ in this study at pH = 6.3. The top of the valence band was obtained by assuming a difference of 0.2 V with the Fermi level potential, and the conduction band energies were deduced from the band-gap values.

4. CONCLUDING REMARKS

It has been successfully demonstrated in our work that $CuAlO_2$ can be synthesized in a nanoporous structure. The nanoporous $CuAlO_2$ products have been characterized in their chemical structures, nanoscopic morphologies, and optical/electrical properties. The success of the sol−gel-based synthesis relies on the initial creation of interpenetrating network structures of inorganic/polymer composite gels in which the polymer gel network prevents significant pore collapse of the inorganic gel network structure during drying, calcination, and annealing of the composite gel. Exploration of the synthetic parameters has led to the conclusions (1) that the annealing temperature needs to be below 1000 °C in order to avoid drastic pore collapse, which could be achieved by annealing in an argon atmosphere, and (2) that $CuAlO_2$ could be prepared in high purity at 900 °C only when the Cu precursor was added in excess. The nanoporous $CuAlO_2$ products produced from our work exhibit the optical and electrical properties consistent with the products in dense or thin film forms reported in the literature. We anticipate that the new nanoporous material is promising for different photoelectrochemical applications because of the combined physical and structural functionalities.

■ AUTHOR INFORMATION

Corresponding Author

*E-mail: dseo@asu.edu. Phone: +1-480-727-7789. Fax: +1-480-965-2747.

Notes

The authors declare no competing financial interest.

■ ACKNOWLEDGMENTS

Conception and the major part of the initial experiments of the synthetic method were supported by the Center for Bio-Inspired Solar Fuel Production, an Energy Frontier Research Center funded by the U.S. Department of Energy, Office of Science, Office of Basic Energy Sciences, under Award DE-SC0001016 and the final characterization of the products was supported by a Multidisciplinary University Research Initiative (MURI) project funded by the Department of Defense through the Army Research Office under Award W911NF-12-1-0420. We thank Daniel Mieritz for the TEM images and gratefully acknowledge the use of facilities within the LeRoy Eyring Center for Solid State Science at Arizona State University.

■ REFERENCES

(1) Gratzel, M. *J. Sol−Gel Sci. Technol.* **2001**, *22*, 7−13.

(2) Franke, M. E.; Koplin, T. J.; Simon, U. *Small* **2006**, *2*, 36−50.

(3) Hou, K.; Puzzo, D.; Helander, M. G.; Lo, S. S.; Bonifacio, L. D.; Wang, W.; Lu, Z.-H.; Scholes, G. D.; Ozin, G. A. *Adv. Mater.* **2009**, *21*, 2492−2496.

(4) Lewis, B. G.; Paine, D. C. *MRS Bull.* **2000**, *25*, 22−27.

(5) Yang, Y.; Wang, L.; Yan, H.; Jin, S.; Marks, T. J.; Li, S. Y. *Appl. Phys. Lett.* **2006**, *89*, 051116.

(6) Emziane, M.; Durose, K.; Halliday, D. P.; Bosio, A.; Romeo, N. *Appl. Phys. Lett.* **2005**, *87*, 251913.

(7) Ginley, D.; Coutts, T.; Perkins, J.; Young, D.; Li, X.; Parilla, P. *MRS Proc.* **2001**, 668.

(8) Müller, V.; Rasp, M.; Rathousky, J.; Schütz, B.; Niederberger, M.; Fattakhova-Rohlfing, D. *Small* **2010**, *6*, 633−637.

(9) Liu, F.; Cardolaccia, T.; Hornstein, B. J.; Schoonover, J. R.; Meyer, T. J. *J. Am. Chem. Soc.* **2007**, *129*, 2446−2447.

(10) Kato, M.; Cardona, T.; Rutherford, A. W.; Reisner, E. *J. Am. Chem. Soc.* **2012**, *134*, 8332−8335.

(11) Volosin, A. M.; Sharma, S.; Traverse, C.; Newman, N.; Seo, D.-K. *J. Mater. Chem.* **2011**, *21*, 13232−13240.

(12) Sharma, S.; Volosin, A. M.; Schmitt, D.; Seo, D.-K. *J. Mater. Chem. A* **2013**, *1*, 699−706.

(13) Simmons, C. R.; Schmitt, D.; Wei, X.; Han, D.; Volosin, A. M.; Ladd, D. M.; Seo, D.-K.; Liu, Y.; Yan, H. *ACS Nano* **2011**, *5*, 6060−6068.

(14) Kwan, P.; Schmitt, D.; Volosin, A. M.; McIntosh, C. L.; Seo, D.-K.; Jones, A. K. *Chem. Commun.* **2011**, *47*, 12367−12369.

(15) Benko, F. A.; Koffyberg, F. P. *J. Phys. Chem. Solids* **1984**, *45*, 57−59.

(16) Kawazoe, H.; Yasukawa, M.; Hyodo, H.; Kurita, M.; Yanagi, H.; Hosono, H. *Nature* **1997**, *389*, 939−942.

(17) Ishiguro, T.; Kitazawa, A.; Mizutani, N.; Kato, M. *J. Solid State Chem.* **1981**, *40*, 170−174.

(18) Park, K.; Ko, K. Y.; Seo, W. S. *J. Eur. Ceram. Soc.* **2005**, *25*, 2219−2222.

(19) Banerjee, A. N.; Chattopadhyay, K. K. *J. Appl. Phys.* **2005**, *97*, 084308.

(20) Shahriari, D. Y.; Barnabè, A.; Mason, T. O.; Poeppelmeier, K. R. *Inorg. Chem.* **2001**, *40*, 5734−5735.

(21) Sato, T.; Sue, K.; Tsumatori, H.; Suzuki, M.; Tanaka, S.; Kawai-Nakamura, A.; Saitoh, K.; Aida, K.; Hiaki, T. *J. Supercrit. Fluids* **2008**, *46*, 173−177.

(22) Kim, K.; Kim, S. S.; Kim, W. S. *Mater. Lett.* **2005**, *59*, 4006−4009.

(23) Hou, L.; Hou, Y. D.; Zhu, M. K.; Tang, H. L.; Liu, J. B.; Wang, H.; Yan, H. *Mater. Lett.* **2005**, *59*, 197−200.

(24) Zhu, X. B.; Dai, J. M.; Li, X. H.; Zhao, B. C.; Liu, S. M.; Song, W. H.; Sun, Y. P. *Mater. Lett.* **2005**, *59*, 2366−2369.

(25) Zhu, X. B.; Yang, J.; Zhao, B. C.; Sheng, Z. G.; Liu, S. M.; Lu, W. J.; Song, W. H.; Sun, Y. P. *J. Phys. D* **2004**, *37*, 2347−2351.

(26) Deng, Z.; Zhu, X.; Tao, R.; Dong, W.; Fang, X. *Mater. Lett.* **2007**, *61*, 686−689.

(27) Dittrich, T.; Dloczik, L.; Guminskaya, T.; Steiner, M. C. L.; Grigorieva, N.; Urban, I. *Appl. Phys. Lett.* **2004**, *85*, 742−744.

(28) Pajonk, G. M. *Appl. Catal.* **1991**, *72*, 217−266.

(29) Rolison, D. R.; Dunn, B. *J. Mater. Chem.* **2001**, *11*, 963−980.

(30) Jacob, K. T.; Alcock, C. B. *J. Am. Ceram. Soc.* **1975**, *58*, 192−195.

(31) Baumann, T. F.; Gash, A. E.; Fox, G. A.; Satcher, J. H., Jr.; Hrubesh, L. W. *Handbook of Porous Solids*; Wiley-VCH: New York, 2002; pp 2014−2037.

(32) Livage, J.; Henry, M.; Sanchez, C. *Prog. Solid State Chem.* **1988**, *18*, 259−341.

(33) Halsey, G. *J. Chem. Phys.* **1948**, *16*, 931.

(34) Faass, G. S. Correlation of Gas Adsorption, Mercury Intrusion and Electron Microscopy Pore Property Data for Porous Glasses. Thesis, Georgia Institute of Technology, Atlanta, GA, 1981.

(35) Schroder, D. K. *Semiconductor Material and Device Characterization*, 3rd ed.; Wiley-VCH: New York, Dec 2005.

(36) Randles, J. E. B. *Discuss. Faraday Soc.* **1947**, *1*, 11−19.

(37) Brug, G. J.; Vanden Eeden, A. L. G.; Sluyters-Rehabach, M.; Sluyters, J. H. *J. Electroanal. Chem.* **1984**, *176*, 275−295.

(38) Renaud, A.; Chavillon, B.; Le Pleux, L.; Pellegrin, Y.; Blart, E.; Boujtita, P. M.; Cario, T. L.; Jobic, S.; Odobel, F. *J. Mater. Chem.* **2012**, *22*, 14353−14356.

(39) Baumann, T. F.; Gash, A. E.; Chinn, S. C.; Sawvel, A. M.; Maxwell, R. S.; Satcher, J. H., Jr. *Chem. Mater.* **2005**, *17*, 395−401.

(40) Thu, T. V.; Thanh, P. D.; Suekuni, K.; Hai, N. H.; Mott, D.; Koyano, M.; Maenosono, S. *Mater. Res. Bull.* **2011**, *46*, 1819−1827.

(41) Götzendörfer, S.; Polenzky, C.; Ulrich, S.; Löbmann, P. *Thin Solid Films* **2009**, *518*, 1153−1156.

(42) Byrne, D.; Cowley, A.; McNally, P.; McGlynn, E. *CrystEngComm* **2013**, *15*, 6144−6150.

(43) Ahmed, J.; Blakely, C. K.; Prakash, J.; Bruno, S. R.; Yu, M.; Wu, Y.; Poltavets, V. V. *J. Alloys Compd.* **2014**, *591*, 275−279.

(44) Ghosh, C. K.; Popuri, S. R.; Mahesh, T. U.; Chattopadhyay, K. K. *J. Sol−Gel Sci. Technol.* **2009**, *52*, 75−81.

DOI: 10.1021/ic5023906
Inorg. Chem. 2015, 54, 1100−1108

(45) Wagner, C. D.; Riggs, W. M.; Davis, L. E.; Moulder, J. F.; Muilenberg, G. E *Handbook of X-Ray Photoelectron Spectroscopy*; Physical Electronics Division, Perkin-Elmer Corp.: Eden Prairie, MN, 1979.

(46) Jolley, L. G.; Geesey, G. G.; Haukins, M. R.; Write, R. B.; Wichlacz, P. L. *Appl. Surf. Sci.* **1989**, *37*, 469−480.

(47) Cai, J.; Gong, H. *J. Appl. Phys.* **2005**, *98*, 033707.

(48) Aston, D. J.; Payne, D. J.; Green, A. J. H.; Egdell, R. G.; Law, D. S. L.; Guo, J.; Glans, P. A.; Learmonth, T.; Smith, K. E. *Phys. Rev. B* **2005**, *72*, 195115.

(49) Pellicer-Porres, J.; Segura, A.; Gilliland, A. S.; Muñoz, A.; Rodríguez-Hernández, P.; Kim, P. D.; Lee, M. S.; Kim, T. Y. *Appl. Phys. Lett.* **2006**, *88*, 181904.

(50) Tate, J.; Ju, H.; Moon, J.; Zakutayev, A.; Richard, A.; Russell, J.; McIntyre, D. *Phys. Rev. B* **2009**, *80*, 165206.

(51) Banerjee, A. N.; Kundoo, S.; Chattopadhyay, K. K. *Thin Solid Films* **2003**, *440*, 5−10.

(52) Nattestad, A.; Zhang, X.; Bach, U.; Cheng, Y.-B. *J. Photonics Energy* **2011**, *1*, 011103.

(53) Bott, A. W. *Curr. Sep.* **1998**, *17*, 87−91.

(54) Benko, F. A.; Koffyberg, F. P. *J. Phys. Chem. Solids* **1984**, *45*, 57−59.

(55) Brahimi, R.; Trari, M.; Bouguelia, A.; Bessekhouad, Y. *J. Solid State Electrochem.* **2010**, *14*, 1333−1338.

(56) Bisquert, J.; Fabregat-Santiago, F. In *Dye Sensitized Solar Cells*; Kalyanasundaram, K., Ed.; Presses Polytechniques et Universitaires Romandes, EPFL: Lausanne, Switzerland, 2010; Chapter 12.

(57) Herraiz-Cardona, I.; Fabregat-Santiago, F.; Renaud, A.; Julián-López, B.; Odobel, F.; Cario, L.; Jobic, S.; Giménez, S. *Electrochim. Acta* **2013**, *113*, 570−574.

(58) Yanagi, H.; Inoue, S.-I.; Ueda, K.; Kawazoe, H.; Hosono, H.; Hamada, N. *J. Appl. Phys.* **2000**, *88*, 4159−4163.

(59) Boschloo, G.; Hagfeldt, A. *J. Phys. Chem. B* **2001**, *105*, 3039−3044.

(60) Fuoco, L.; Joshi, U. A.; Maggard, P. A. *J. Phys. Chem. C* **2012**, *116*, 10490−10497.

(61) Xu, Y.; Schoonen, A. A. *Am. Mineral.* **2000**, *85*, 543−556.

(62) Morrison, S. R. *Electrochemistry at semiconductor and oxidized metal electrodes*; Plenum: New York, 1980; p 62.

(63) Kawazoe, H.; Yanagi, H.; Ueda, K.; Hosono, H. *Mater. Res. Bull.* **2000**, *25*, 28−36.

(64) Prakash, T.; Padma Prasad, K.; Kavitha, R.; Ramasamy, S.; Murty, B. S. *J. Appl. Phys.* **2007**, *102*, 104104.